HCO Quantum Yields in the Photolysis of HC(O)C(O)H (Glyoxal) between 290 and 420 nm

Karl J. Feierabend,[†,‡] Jonathan E. Flad,[†,‡,§] S. S. Brown,[†] and James B. Burkholder*[,†]

Earth System Research Laboratory, Chemical Sciences Division, National Oceanic and Atmospheric Administration, 325 Broadway, Boulder, Colorado 80305-3328, and Cooperative Institute for Research in the Environmental Sciences, University of Colorado, Boulder, Colorado 80309

Received: April 9, 2009; Revised Manuscript Received: May 15, 2009

Quantum yields, Φ, for the production of the formyl radical, HCO, in the photolysis of glyoxal were determined at 85 wavelengths, λ, in the range of 290−420 nm at pressures between 50 and 550 Torr (N_2) at 298 K using pulsed-laser photolysis combined with cavity ring-down spectroscopy detection of HCO. HCO quantum yields were parametrized using a Stern−Volmer analysis to obtain extrapolated zero-pressure HCO quantum yields, $\Phi_0(\lambda)$, and values for the ratio of the rate coefficients for quenching and dissociation, $k_q/k_d(\lambda)$, at each wavelength. $\Phi_0(\lambda)$ varied smoothly with wavelength with a maximum value of ∼1.8 in the range 300−385 nm with values decreasing to near 0 at 420 nm and 0.4 at 290 nm. $k_q/k_d(\lambda)$ was measurable at nearly all photolysis wavelengths and is well-represented by the relationship $k_q/k_d(\lambda) = (2.3 \times 10^{-20}) + (1.5 \times 10^{-19}) \exp(-0.4\Delta E)$ (cm^3 molecule $^{-1}$) where $\Delta E = ((28\,571/\lambda) - 72.5)$ (kcal mol^{-1}), λ is the photolysis wavelength (nm), and 72.5 kcal mol^{-1} is the threshold for glyoxal photodissociation. Differences in our HCO quantum yield wavelength- and pressure-dependence with previous studies are discussed. The present HCO quantum yield data are appropriate for use in atmospheric model calculations, and revised wavelength-dependent photolysis branching ratios for the production of 2HCO, $H_2CO + O_2$, and $H_2 + 2CO$ at atmospheric pressure are presented.

I. Introduction

Glyoxal, HC(O)C(O)H, is a stable end product formed in the atmosphere via oxidation of a variety of volatile organic compounds (VOCs).[1−5] Once formed in the atmosphere, glyoxal is relatively short-lived, with an estimated lifetime of several hours. The two primary gas-phase atmospheric loss processes for glyoxal are photolysis in the UV/vis wavelength region and reaction with the OH radical.[6−8] The actual atmospheric lifetime of glyoxal is therefore highly dependent on the time and location of its formation. We recently reported a detailed study of the OH + glyoxal reaction rate coefficient over the temperature range of 210−390 K and found $k(T) = [(6.5 \pm 0.9) \times 10^{-18}]T^2[\exp([820 \pm 30]/T)]$ cm^3 molecule^{-1} s^{-1}.[6] Whereas the atmospheric lifetime of glyoxal with respect to the OH reaction is short, ∼6 h, UV/vis photolysis will most likely dominate its loss during the daytime with an estimated lifetime of ∼2 to 3 h. At night, glyoxal could potentially be removed via reaction with NO_3; however, this reaction is expected to be slow and, therefore, a minor loss process under typical atmospheric conditions. Understanding the relative lifetimes for the two major glyoxal loss processes is important, as shown in Figure 1, because UV/vis photolysis most likely leads to net HO_x production in the atmosphere, whereas reaction with OH does not. Because tropospheric HO_x ($HO_x = OH + HO_2$) influences regional ozone formation and air quality, determining the rates for these two loss processes is needed to quantify glyoxal's contribution to the oxidative capacity of the atmosphere. In addition, it has been suggested that glyoxal may also play a role in secondary organic aerosol formation in polluted urban environments.[9]

The atmospheric abundance of glyoxal has been measured in the boundary layer and found to be variable depending on time and location with average daytime values in the range of 0.03 to 1.8 ppb.[9−12] Satellite measurements[13] have also been used to survey the glyoxal abundance on the global scale, where the annual mean column of glyoxal has been found to be in the range ∼10^{14} to 10^{15} molecules cm^{-2}, which is roughly consistent with global model calculations.[14] Improving the accuracy of kinetic and photochemical parameters for glyoxal's atmospheric loss processes will help quantify global sources and sinks.

Glyoxal is the simplest dialdehyde, however, its photochemistry is rather complex and not as well understood as that of many monoaldehydes. Several photolysis pathways for glyoxal are energetically accessible from solar radiation

$$\mathrm{HC(O)C(O)H} + h\nu \rightarrow \mathrm{H} + \mathrm{HC(O)CO} \quad \lambda_T = 337\ \mathrm{nm} \tag{1a}$$

$$\rightarrow \mathrm{HCOH} + \mathrm{CO} \quad \lambda_T = 591\ \mathrm{nm} \tag{1b}$$

$$\rightarrow \mathrm{HCO} + \mathrm{HCO} \quad \lambda_T = 399\ \mathrm{nm} \tag{1c}$$

$$\rightarrow \mathrm{H_2CO} + \mathrm{CO} \quad \text{all } \lambda \tag{1d}$$

$$\rightarrow \mathrm{H_2} + \mathrm{CO} + \mathrm{CO} \quad \text{all } \lambda \tag{1e}$$

where λ_T (nm) is the energetic threshold for each channel calculated using the heats of formation, $\Delta_f H$(298 K), given in

* Corresponding author. E-mail: James.B.Burkholder@noaa.gov.
† National Oceanic and Atmospheric Administration.
‡ University of Colorado.
§ Current address. The Ohio State University, Agricultural Technical Institute, Wooster, OH, 44691.

10.1021/jp9033003 CCC: $40.75
Published on Web 06/12/2009

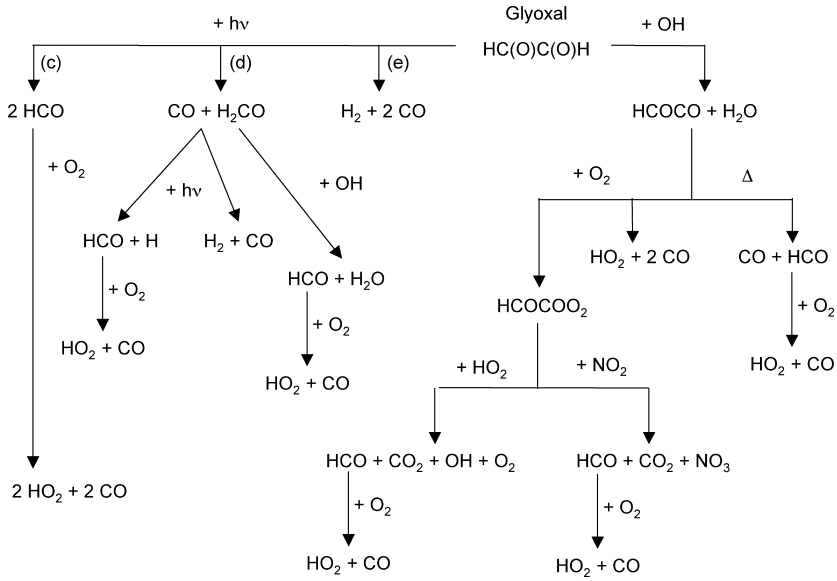

Figure 1. Atmospheric degradation scheme for glyoxal showing HO_x production via UV/vis photolysis and the OH reaction.[6,15,18] OH-initiated oxidation of glyoxal does not lead to net HO_x production. The HO_x production in the UV/vis photolysis is dependent on the photolysis product branching ratios. The branching ratio for the loss of glyoxal favors UV/vis photolysis over OH reaction under typical daylight atmospheric conditions.[6−8]

Sander et al.[15] for channels 1c, 1d, and 1e and taken from the theoretical works of Li et al.[16] and Koch et al.[17] for channels 1a and 1b. The HC(O)C(O) radical formed in channel 1a undergoes rapid thermal unimolecular decomposition

$$HC(O)C(O) \rightarrow HCO + CO \qquad (2)$$

where k_2(298 K) has been estimated to be 3.2×10^7 s^{-1}.[18] This is important for the present work, which detects HCO as a photolysis product. The formation of the HCOH radical in channel 1b is expected to be minor at all wavelengths.[19]

The focus of the present work is on the quantification of the radical production channels, 1a and 1c, that are important to atmospheric HO_x production. The rupture of the carbon−carbon bond occurs via a Norrish type I reaction that is typical in aldehyde and ketone photochemistry. However, the molecular elimination channels (Norrish type II reactions), 1d and 1e, are also known to occur and compete with the radical production channels at some photolysis wavelengths.[8] However, previous studies have shown that photolysis of glyoxal forming HCO dominates under atmospheric conditions,[8] indicating the importance of the radical production channels.

The UV/vis absorption spectrum of glyoxal, important for understanding its atmospheric photolysis, is shown in Figure 2. The spectrum in this wavelength range shows two distinct absorption regions: a broad absorption feature that peaks near 300 nm and a more finely structured region peaking near 450 nm. The absorption features correspond to transitions to an excited singlet state and much weaker transitions to an excited triplet state. Thermodynamic thresholds indicated in Figure 2 provide qualitative guidelines for understanding glyoxal's atmospheric photolysis and radical production rates. Figure 3 shows an illustration of a cut along glyoxal's potential energy surfaces leading to the formation of HCO. Photodissociation to form HCO can occur via multiple channels (1a and 1c) and from multiple potential energy surfaces, illustrating the complexity of interpreting HCO quantum yield data. Two previous studies have investigated glyoxal's potential energy surfaces in the context of photodissociation to form HCO. Chen et al.[20]

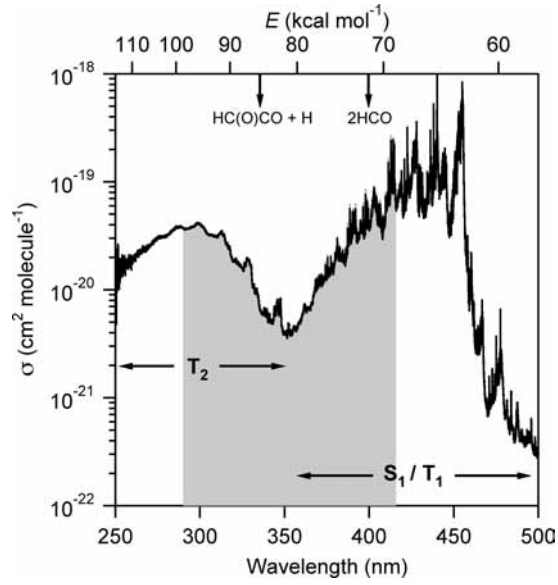

Figure 2. Absorption spectrum of glyoxal recorded at 0.001 nm resolution by Volkamer et al.[25] The shaded portion denotes the wavelength region for the HCO quantum yields investigated in the present study (290−420 nm). The regions corresponding to the electronic states of glyoxal are notated "S" for singlet and "T" for triplet. The vertical arrows represent the thermodynamic thresholds for photolysis channels 1a (HCOCO + H) and 1c (HCO + HCO).[15,16]

quantified an energetic threshold for HCO formation on glyoxal's triplet (T_1) surface at 72.5 kcal mol^{-1} (394.4 nm). (See Figure 3.) The ab initio study of Li et al.,[16] which characterized excited-state potential energy surfaces of glyoxal, was in good agreement with the laboratory study of Chen at al. These studies provide a qualitative guide to interpreting the HCO quantum yield results because glyoxal's photodynamics above and below the T_1 barrier most likely exhibit different behavior.

There are several studies that have examined the photolysis quantum yields of glyoxal.[8,21−23] However, discrepancies exist for the wavelength dependence and magnitude of the HCO quantum yield. Here we report wavelength-dependent quantum yields for the formation of HCO in the UV photolysis of glyoxal,

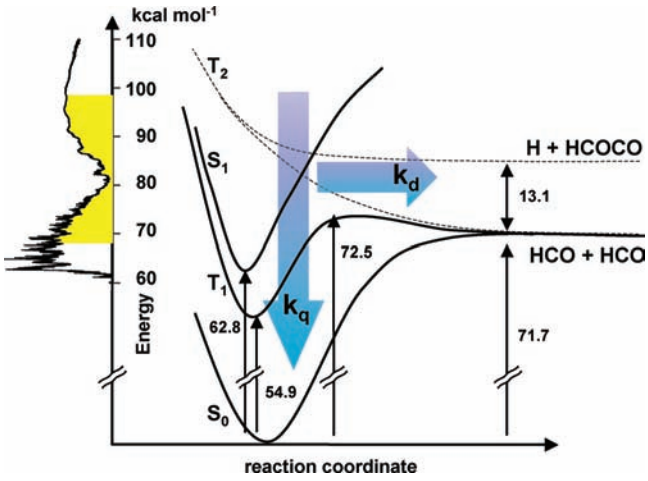

Figure 3. Illustration adapted from Chen et al.[21] showing the electronic-state potential energy surfaces (PESs) of glyoxal, transition energies, and pathways leading to HCO photolysis products, channels 1a and 1c. Energies are relative to the zero-point energy in the ground electronic (S_0) state. A qualitative T_2 potential energy surface is shown to include possible pathways from the short wavelength absorption band to the HCO photolysis product. The glyoxal absorption spectrum is shown along the *y* axis to illustrate its correlation with the PES, where the highlighted region is the range of wavelengths included in our HCO quantum yield measurements.

channels 1a and 1c. Quantum yields were measured over the wavelength range of 290−420 nm at pressures between 50 and 550 Torr (N_2) at 298 K using a tunable pulsed-laser photolysis−cavity ring-down spectroscopy (PLP-CRDS) technique recently developed in our laboratory.[24] The sensitivity and versatility of this PLP-CRDS technique enables an accurate determination of the HCO quantum yield over the wavelength range and pressures relevant for atmospheric photolysis rate calculations. Following the presentation of our HCO quantum yield measurements, we have combined our results with those from Tadic et al.[8] to provide a revised recommendation for glyoxal photolysis branching ratios as a function of wavelength at atmospheric pressure for use in atmospheric model calculations.

II. Experimental Section

In this study, the quantum yield for HCO formation, Φ_{HCO}, in the pulsed-laser photolysis (PLP) of glyoxal was determined relative to a well-characterized reference photolysis system. HCO quantum yields were measured at room temperature at 85 photolysis wavelengths between 290 and 420 nm using tunable PLP of glyoxal combined with cavity ring-down spectroscopy (CRDS) for the detection of HCO.[24] The pressure dependence of the HCO quantum yield was measured at each photolysis wavelength using bath gas pressures in the range of 50−550 Torr with N_2 as the bath gas. A schematic of the experimental apparatus is shown in Figure 4, and this section describes the experimental details and methods used to obtain the HCO quantum yields. The apparatus has been used in recent studies from this laboratory, and additional details can be found elsewhere.[24]

HCO quantum yields were measured using a collinear tunable laser photolysis−cavity ring-down setup. The flow reactor was constructed from a 1.7 cm i.d. stainless steel cylinder that was coupled to highly reflective mirrors mounted at either end to create the optical cavity. The CRDS mirrors were highly reflective in the visible (600−650 nm) and transmissive in the UV region (290−440 nm). The pulsed CRDS probe and photolysis beams counter-propagated collinearly through the length of the reactor and nominally operated at 10 Hz. The CRDS probe beam was generated by a Nd/YAG pumped dye laser. The beam exiting the dye laser was focused to a diameter of ∼1 mm and maintained at an energy of ∼1 mJ pulse^{-1} before entering the optical cavity. Light exiting the rear mirror of the optical cavity was collected and averaged on a 16-bit waveform digitizer at a sample rate of 1 MHz. The wavelengths of the probe and photolysis beams were measured using a laser wavelength meter to an accuracy of 0.01 nm. All wavelengths reported are in air. HCO quantum yields were measured using CRDS probe wavelengths near ∼615 nm, as in our previous HCO absorption spectrum and quantum yield measurements.[24]

Cavity ring-down spectroscopy is a highly sensitive technique that can be used to measure the absorption of transient species. The cavity ring-down time constant, τ, is related to the absorption coefficient, $\alpha(\lambda)$ (cm^{-1}), by the relationship

$$\alpha_t(\lambda) = [\mathrm{HCO}]_t \sigma_{\mathrm{HCO}}(\lambda) = \frac{l_{\mathrm{cavity}}}{l_{\mathrm{absorb}} c}\left(\frac{1}{\tau_t(\lambda)} - \frac{1}{\tau_0(\lambda)}\right) \qquad (3)$$

where λ is the wavelength of the CRDS probe beam, $\sigma_{HCO}(\lambda)$ is the absorption cross section (cm^2 molecule^{-1}) of HCO at wavelength λ, l_{cavity} is the cavity path length (cm), l_{absorb} is the path length (cm) for the absorbing sample, c is the speed of light, and $\tau_t(\lambda)$ and $\tau_0(\lambda)$ are the ring-down time constants with and without the absorber present, respectively, and t is the delay after the photolysis laser pulse. In the configuration used in this study $l_{cavity} = 100 \pm 1$ cm and $l_{absorb} = 63 \pm 3$ cm. The l_{absorb} value was determined in our previous study.[24] The CRDS mirrors had τ_0 values of ∼40 μs in the absence of the UV photolysis beam. The τ_0 values decreased in the presence of the photolysis beam to ∼25 μs. Ring-down time constants were typically measured over at least three lifetimes, and at least 1000 individual measurements (i.e., laser shots) of τ were averaged for each experiment to determine $\alpha(\lambda)$.

The photolysis beam made a single pass through the reactor, passing through the CRDS mirrors, collinear to the optical cavity. Photolysis wavelengths in the range of 290−420 nm were generated using the frequency-doubled output of a pulsed Nd/YAG pumped dye laser using a BBO crystal. The line width of the photolysis laser was ∼0.001 nm (0.1 cm^{-1}). The power of the photolysis beam in the reactor was varied over the range of 0.5−4 mJ pulse^{-1}, ∼5 mm beam diameter, during the course of the experiments. The photolysis laser power was kept at <4 mJ pulse^{-1} to avoid damaging the CRDS mirrors. The photolysis beam power was monitored using a single-shot power meter at the exit of the reactor. The power reading was used to monitor and normalize the measured $\Phi(\lambda)$ values for variations in laser power (typically <10%) during the course of an experiment that typically lasted ∼15 min. The delay between the photolysis and probe beams could be varied from 5 μs to 100 ms. A minimum delay time of 5 μs was used to avoid scattered light interference from the photolysis laser. In many experiments, the wavelength of the photolysis laser was stepped over a narrow wavelength range, 5−15 nm while recording the CRDS signal and holding the experimental conditions (flows, concentrations, and pressure) constant. An autotracker was used to optimize and maintain the stability of the power output of the frequency-doubled light during the photolysis scan.

HCO photolysis quantum yields were determined using a relative method. The advantage of using a relative method is the minimization of errors associated with determining the absolute HCO concentration and calibration of the photolysis laser fluence. The relative method therefore improves the

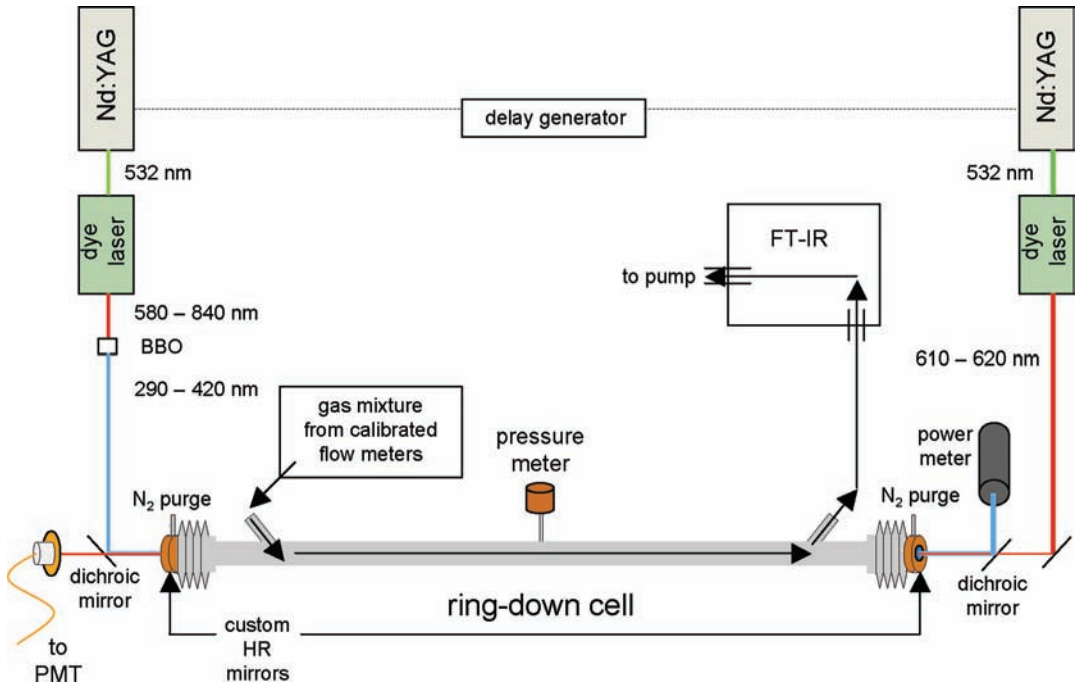

Figure 4. Schematic of the collinear pulsed-laser photolysis−cavity ring-down spectroscopy apparatus used to measure HCO quantum yields.

precision and accuracy of the quantum yield measurements provided that an accurate reference system is available. In this study, HCO quantum yields were measured relative to HCO produced following the photolysis of mixtures of Cl_2 and H_2CO

$$Cl_2 + h\nu \rightarrow Cl + Cl \tag{4}$$

where the quantum yield for Cl atom production, Φ_{Cl_2}, is 2 for all photolysis wavelengths used in our work[15] and

$$Cl + H_2CO \rightarrow HCO + HCl \tag{5}$$

where $k_5(298\ K) = 7.3 \times 10^{-11}$ cm^3 molecule^{-1} s^{-1}.[15] The formation of Cl atoms in reaction 4 leads to a stoichiometric amount of HCO being formed via reaction 5. H_2CO concentrations of $\geq 8 \times 10^{15}$ molecules cm^{-3} were used so that reaction 5 was >99% complete within 5 μs, which is instantaneous on the time scale of the CRDS measurements. The HCO radical concentration produced in this system, $[HCO]_{Cl_2}(\lambda)$, is given by

$$[HCO]_{Cl_2}(\lambda) = [Cl_2]\sigma_{Cl_2}(\lambda)\Phi_{Cl_2}F(\lambda) \tag{6}$$

where $\sigma_{Cl_2}(\lambda)$ is the absorption cross section of Cl_2 at the photolysis wavelength, λ, and F is the photolysis laser fluence in units of photon cm^{-2} pulse^{-1}. Note that the formation of HCO in this reference system is independent of pressure.

The HCO radical concentration formed in the PLP of glyoxal, $[HCO]_g(\lambda,P)$, is given by a similar relationship

$$[HCO]_g(\lambda, P) = [\text{glyoxal}]\sigma_g(\lambda)\Phi_{HCO}(\lambda, P)F(\lambda) \tag{7}$$

where $\sigma_g(\lambda)$ is the glyoxal absorption cross section (cm^2 molecule^{-1}) at the photolysis wavelength. Note that in this case, the HCO formation is pressure dependent because of the pressure dependence in the HCO quantum yield in the photolysis of glyoxal. The UV absorption cross sections for glyoxal, $\sigma_g(\lambda)$, and Cl_2, $\sigma_{Cl_2}(\lambda)$, were taken from Volkamer et al.[25] and Maric et al.,[26] respectively.

Combining eqs 6 and 7 yields the HCO quantum yield, $\Phi_{HCO}(\lambda,P)$

$$\Phi_{HCO}(\lambda, P) = \frac{[HCO]_g(\lambda, P)}{[HCO]_{Cl_2}(\lambda)} \frac{[Cl_2]}{[\text{glyoxal}]} \frac{\sigma_{Cl_2}(\lambda)}{\sigma_g(\lambda)} \Phi_{Cl_2} \tag{8}$$

in terms of the measured HCO and precursor concentrations combined with well-known absorption cross sections and source chemistry. In eq 8, the photolysis laser fluence cancels provided that it is constant between the sample and reference measurements. Experimentally, the absorption coefficient, α_0, which is proportional to $[HCO]_0$, was measured; that is, the determination of the absolute HCO radical concentration is not required. $\Phi_{HCO}(\lambda,P)$ was determined in a series of back-to-back measurements that included the photolysis of glyoxal and the reference system. Performing experiments in a back-to-back sequence enabled the photolysis laser fluence and other experimental parameters (such as gas flows and pressures) to be held nearly constant during the Φ_{HCO} determination. Expressing eq 8 in terms of the experimentally measured quantities yields

$$\Phi_{HCO}(\lambda, P) = \frac{\alpha_0^g(\lambda, P)}{\alpha_0^{Cl_2}(\lambda)} \frac{[Cl_2]}{[\text{glyoxal}]} \frac{\sigma_{Cl_2}(\lambda)}{\sigma_g(\lambda)} \Phi_{Cl_2} \tag{9}$$

Quantum yields were determined directly from this equation at a fixed [glyoxal] for each experiment. In a small number of experiments, quantum yields were determined from the slope of α_0^g versus [glyoxal] to confirm linearity. The ratio of $[Cl_2]/\alpha_0^{Cl_2}$ was obtained for each experiment and at each wavelength from calibrations in which the $[Cl_2]$ was varied over a factor of ~10 while holding the photolysis laser fluence and $[H_2CO]$ constant.

For photolysis wavelengths <330 nm, the photodissociation of H_2CO in the reference system produces an instantaneous HCO signal

$$H_2CO + h\nu \rightarrow HCO + H \quad (10a)$$

$$'H_2 + CO \quad (10b)$$

where the branching ratio for channel 10a is ~50% over the range of wavelengths used in this study.[15] The "background" HCO absorption signal remained constant during a calibration measurement by maintaining a constant $[H_2CO]$. The H_2CO concentration was monitored during an experiment using online Fourier transform infrared absorption that is described later. The HCO absorption signal appeared as an intercept (≤25% of the total signal) in $[Cl_2]$ versus $\alpha_0^{Cl_2}$ and was consistent with photolysis of H_2CO in the absence of Cl_2. We minimized the HCO signal by selecting photolysis wavelengths corresponding to minima in the H_2CO absorption spectrum whenever possible.

In both the sample and reference photolysis systems, we measured the loss of the HCO radical by varying the delay between the photolysis laser pulse and the CRDS probe laser pulse. Under all conditions, the loss of HCO was observed to be first-order

$$\ln([HCO]_t/[HCO]_0) = -(\sum k_x[X] + k_d)t = k't \quad (11)$$

where k' represents a first-order rate coefficient for the loss of HCO, k_x is the first-order rate coefficient for the gas-phase reaction of HCO with compound X, and k_d is the first-order rate coefficient for diffusion of HCO out of the detection volume. Experimentally measured values of k' were in the range of 200−800 s^{-1}, with the higher values observed at higher pressure, and are consistent with an O_2 impurity in the gas flow of approximately 5−20 ppm

$$HCO + O_2 \rightarrow HO_2 + CO \quad (12)$$

where $k_{12}(298\ K) = 5.2 \times 10^{-12}$ cm^3 $molecule^{-1}$ s^{-1}.[15] In the reference system, the reaction with Cl_2

$$HCO + Cl_2 \rightarrow HC(O)Cl + Cl \quad (13)$$

where $k_{13}(298\ K) = 7.6 \times 10^{-12}$ cm^3 $molecule^{-1}$ s^{-1} also occurred.[27] Note that the HCO loss does not influence the interpretation of the HCO quantum yield data provided that the losses are small on the time scale of the CRDS measurement, as described in a previous study.[24] Over the time interval of a typical CRDS measurement, ~3τ, the HCO concentration decayed <5% in the worst case and was negligible in most experiments. The HCO signal obtained with a 5 μs photolysis−probe delay time was used in the final data analysis.

Materials. Glyoxal was introduced to the gas flow from dilute gas mixtures of glyoxal in N_2. We determined the glyoxal concentration in the reactor by using online infrared absorption and the gas flow rates from the manometrically prepared glyoxal/N_2 mixtures. Infrared absorption spectra were recorded between 500 and 4000 cm^{-1} using a Fourier transform spectrometer at a spectral resolution of 1 cm^{-1} in 50 coadded scans. The infrared absorption spectra were measured either before or after the reactor. A multipass absorption cell (485 cm optical path length, 750 cm^3 total volume, KBr windows) was used for the infrared measurements. Infrared absorption cross sections for glyoxal of 8.11×10^{-19} cm^2 $molecule^{-1}$ for the peak of the C═O stretch, R branch (1740 cm^{-1}), and the integrated band strength of 1.63×10^{-17} cm^2 $molecule^{-1}$ cm^{-1} for the C−H band (2724−2940 cm^{-1}) were taken from Feierabend et al.[6] The concentrations determined from the infrared measurements were scaled to account for dilution and differences in pressure between the reactor and absorption cells to obtain the concentrations within the reactor. The glyoxal concentration was varied over the range ~10^{14}−10^{16} molecules cm^{-3} during the HCO quantum yield measurements.

Cl_2 was introduced to the reactor gas flow from one of two commercial gas mixtures of Cl_2 in He, 0.2607%, and Cl_2 in N_2, 0.203%. The mixture was added to the reactor gas flow through a calibrated flow meter, and $[Cl_2]$ was determined using the measured flow rate and sample mixing ratio. The H_2CO concentration was determined using online infrared absorption, as described above using the integrated infrared band strengths reported by Nakanaga et al.[28] The H_2CO and Cl_2 concentrations were in the range of $(8-20) \times 10^{15}$ and $(3-100) \times 10^{13}$ molecules cm^{-3}, respectively, during the reference calibration measurements.

N_2 (UHP, >99.99%), O_2 (UHP, >99.99%), and Cl_2/N_2 mixtures were used as supplied. We prepared formaldehyde, H_2CO, online by thermally cracking a sample of 1,3,5-trioxane (>99%). A small flow of N_2 (~30 STP cm^3 min^{-1}) was passed over the sample and into a small glass oven (0.5" o.d. × 7.5") maintained at 400 K. A trap maintained at 195 K after the oven prevented nonvolatile impurities from entering the reactor.

Glyoxal was obtained commercially in a stable hydrated form (glyoxal trimer−dihydrate, ≥95%). Pure glyoxal monomer was prepared from the solid trimer−dihydrate using the methods described by Volkamer et al.[25] where equal masses (~5 g) of glyoxal trimer−dihydrate and solid phosphorus pentoxide (P_2O_5, ≥98%) were mixed and slowly heated under vacuum from 298 to ~433 K. A small flow of N_2 (~20 STP cm^3 min^{-1}) was passed over the heated sample and through a trap, where the bright-yellow pure glyoxal solid was collected at 195 K. The glyoxal sample was used without further purification. Glyoxal/N_2 mixtures were prepared manometrically in darkened 12 L Pyrex bulbs. The glyoxal/N_2 mixtures were added to the reactor gas flow through a calibrated flow meter. Several gas mixtures were prepared over the course of the study with glyoxal mixing ratios between ~0.5 and 3% and initial total pressures of ~1000 Torr (N_2). The mixtures were stable over a period of at least three weeks, as also found in our previous kinetic study.[6]

Calibrated electronic mass flow transducers were used to measure gas flows. The total gas flow rate through the reactor was ~2000 STP cm^3 min^{-1}. To ensure that the reactor contained no absorbing species at the CRDS probe wavelength from previous photolysis pulses, measurements of ring-down time constant (τ) were routinely made with the CRDS probe pulse occurring 50 μs prior to the photolysis pulse. These measurements showed no difference in τ with the photolysis source on or off. Pressures were measured with calibrated 1000 Torr capacitance manometers. All experiments were conducted at ambient temperature, ~296 K, with N_2 as the bath gas.

III. Results and Discussion

HCO quantum yields from the photolysis of glyoxal were determined at 85 wavelengths in the range of 290−420 nm at bath gas pressures between 50 and 550 Torr (N_2). The measured HCO absorption coefficients, α_0^g, were found experimentally

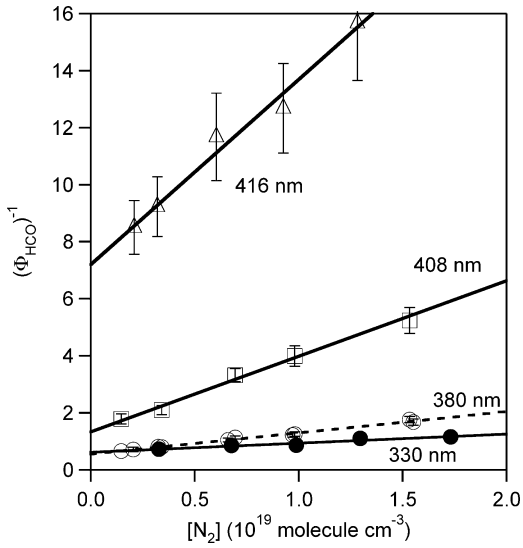

Figure 5. Representative HCO quantum yield data measured in the photolysis of glyoxal at 330 (●), 380 (○), 408 (□), and 416 nm (△) and the Stern−Volmer analysis, eq 14 (lines). The slope yields $k_q/k_d(\lambda)$ and the intercept Φ^0_{HCO}, both of which are wavelength dependent. The error bars are the 2σ (95% confidence) level precision errors of the measurement.

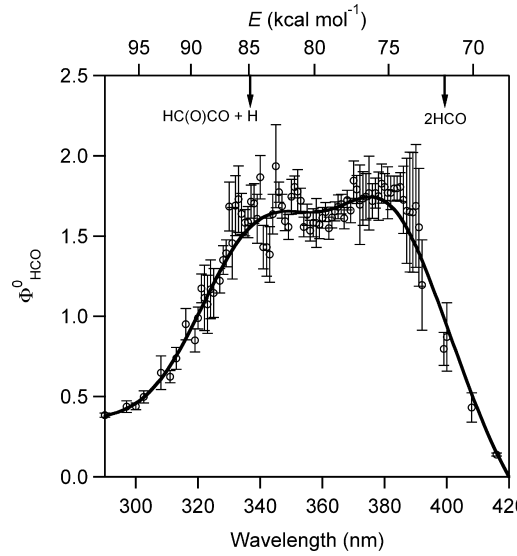

Figure 6. Summary of the zero-pressure HCO quantum yield, Φ^0_{HCO}, values obtained in this work from the UV/vis photolysis of glyoxal. The zero-pressure HCO quantum yields were obtained from weighted linear-least-squares fits of experimental values obtained over the pressure range of 50−550 Torr (N_2) at 296 to a Stern−Volmer equation, eq 14. The data shown here are also given in Table 1. The error bars are the precision fit error at the 2σ confidence level. The solid trace is an interpolation of the data. (See Table S2 in the Supporting Information for the interpolated values.) The vertical arrows represent the thermodynamic thresholds for photolysis channels 1a (HCOCO + H) and 1c (HCO + HCO).[15,16]

to vary linearly with [glyoxal] and the photolysis laser fluence, as shown in Figure S1 in the Supporting Information. The observed linearity is consistent with the expected relationship given in eqs 3 and 7. The HCO quantum yield at each photolysis wavelength was measured at five or more total pressures while maintaining an approximately constant glyoxal concentration. The pressure dependence of the HCO quantum yield was parametrized using a standard Stern−Volmer relationship

$$\frac{1}{\Phi_{HCO}(\lambda, P)} = \frac{1}{\Phi^0_{HCO}(\lambda)} + \frac{k_q}{k_d}(\lambda)[N_2] \qquad (14)$$

where Φ^0_{HCO} represents the HCO quantum yield in the zero pressure limit, k_q is a second-order rate coefficient representing the effective collisional quenching of glyoxal out of the excited electronic state or below the threshold for dissociation by N_2, and k_d is an effective first-order rate coefficient representing all processes leading to dissociation of glyoxal to form HCO. k_q and k_d are both expected to be wavelength dependent, but our measurements are only sensitive to the ratio of the rate coefficients. A weighted linear-least-squares fit of $(\Phi_{HCO}(\lambda,P))^{-1}$ versus $[N_2]$ yielded $k_q/k_d(\lambda)$ from the slope and $\Phi^0_{HCO}(\lambda)$ from the intercept. A summary of all measured quantum yield data is given in Table S1 in the Supporting Information.

Representative experimental $\Phi_{HCO}(\lambda,P)$ data and Stern−Volmer analyses are shown in Figure 5 for several photolysis wavelengths, including the extremes of our measurements. The Stern−Volmer relationship reproduces the experimentally measured values very well for all photolysis wavelengths. The precision error for the Stern−Volmer intercepts, Φ^0_{HCO}, was usually ≤10% at the 2σ (95% confidence) level but increased somewhat in the threshold region where the HCO quantum yields were smallest. The slopes from the Stern−Volmer analyses typically had precision errors of 20%. The precision error in the slope increased to ≥50% at the shortest photolysis wavelengths where the values for $k_q/k_d(\lambda)$ were $<4 \times 10^{-20}$ cm^3 $molecule^{-1}$.

The results of the Stern−Volmer analyses are given in Table 1 and are shown in Figures 6 and 7, where $\Phi^0_{HCO}(\lambda)$ and $k_q/k_d(\lambda)$ are plotted as a function of photolysis wavelength, respectively. Over the range of photolysis wavelengths included in this study and the spacing of the data, $\Phi^0_{HCO}(\lambda)$ was found to vary smoothly as a function of photolysis wavelength; that is, within the precision of the measurements, there are no apparent features due to the vibrational band structure in the glyoxal absorption spectrum. $\Phi^0_{HCO}(\lambda)$ shows a dependence on the photolysis wavelength with three distinct regions clearly visible in the data shown in Figure 6 that correlate with the glyoxal photolysis channel thresholds for reactions 1a and 1c. Starting at the long wavelength limit of our measurements, $\Phi^0_{HCO}(\lambda)$ increases from a small value of 0.14 ± 0.02 (2σ) at 416 nm to a maximum value of 1.80 ± 0.20 (2σ) at 385 nm. This wavelength region corresponds to the transition through the threshold for the formation of 2HCO in channel 1c. $\Phi^0_{HCO}(\lambda)$ is nearly constant in the range 385−330 nm and then decreases smoothly to a value of ∼0.4 at 290 nm. The decrease in $\Phi^0_{HCO}(\lambda)$ starting near 330 nm correlates with the threshold for channel 1a and the onset of HC(O)C(O) + H production. In summary, the quantum yield for HCO formation is large over the range of atmospherically relevant wavelengths, which is consistent with previous studies that found channel 1c to be dominant under atmospheric conditions.[8,21] However, Φ^0_{HCO} never reaches the maximum possible value of 2, suggesting the presence of other photolysis channels at these wavelengths, assuming a glyoxal photolysis quantum yield of unity. We will return to this point in the Atmospheric Implications section.

The obtained $k_q/k_d(\lambda)$ values are shown in Figure 7. At long wavelengths near the threshold for channel 1c, $k_q/k_d(\lambda)$ decreases rapidly with decreasing wavelength, as expected, with $k_q/k_d(\lambda)$ values in the threshold region between (6 and 2) $\times 10^{-19}$ cm^3 $molecule^{-1}$. Assuming a relatively efficient collision quenching rate coefficient of 1×10^{-11} cm^3 $molecule^{-1}$ s^{-1}, this corre-

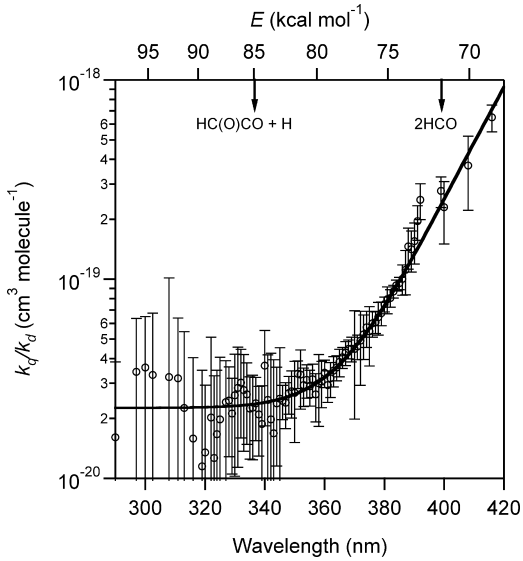

Figure 7. Summary of k_q/k_d values obtained from a Stern−Volmer analysis, eq 14, of the HCO quantum yield data obtained in the UV/vis photolysis of glyoxal. The k_q/k_d values were obtained from weighted linear least-squares fits of quantum yield values obtained over the pressure range 50−500 Torr (N_2) at 296 K. Error bars represent precision error at the 2σ confidence level. The solid line is an empirical fit to the data: $k_q/k_d(\lambda) = (2.3 \times 10^{-20}) + (1.5 \times 10^{-19}) \exp(-0.4\Delta E)$, where $\Delta E = ((28\,571/\lambda) - 72.5)$ (kcal mol^{-1}), λ is the excitation wavelength (nm), and 72.5 kcal mol^{-1} is the threshold for glyoxal photodissociation. The vertical arrows represent the thermodynamic thresholds for photolysis channels 1a (HCOCO + H) and 1c (HCO + HCO).[15,16]

sponds to excited-state lifetimes ($1/k_d$) in the range of 60−20 ns. Toward shorter wavelengths, $k_q/k_d(\lambda)$ decreases to an asymptotic value of $\sim 2 \times 10^{-20}$ cm^3 molecule^{-1} near 350 nm, which is consistent with an excited-state lifetime of ~2 ns. The lifetime of the glyoxal excited state implies that photodissociation is not instantaneous and is consistent with the complex photodynamics outlined in Figure 3. The wavelength dependence of k_q/k_d is described very well by an exponential function in terms of the excitation energy above the T_1 barrier for production of 2HCO (72.5 kcal mol^{-1})

$$\frac{k_q}{k_d}(\lambda) = (2.3 \times 10^{-20}) + (1.5 \times 10^{-19}) \exp(-0.4\Delta E) \qquad (15)$$

where $\Delta E = ((28\,571/\lambda) - 72.5)$ (kcal mol^{-1}) and λ is the excitation wavelength (nanometers). The $k_q/k_d(\lambda)$ values at all wavelengths are significant and influence atmospheric photolysis rate calculations, as described in the Atmospheric Implications section.

In addition, there are several other key features in the quantum yield data that are worth pointing out. First, at the longest photolysis wavelength included in this study, 416 nm, which is 3.0 kcal mol^{-1} below the thermodynamic threshold for production of HCO + HCO, we obtain a statistically significant nonzero value for Φ^0_{HCO} of 0.14 ± 0.02. From a purely thermodynamic point of view, the source of HCO at these low excitation energies is unexpected unless glyoxal in vibrationally excited levels in the ground electronic state has significantly higher absorption cross sections than the ground vibrational state. The temperature dependence of the HCO quantum yield in the threshold region would help address this question but was not within the scope of the present study. Second, in our experiments, we measure the total HCO production and do not distinguish between channels 1a and 1c. Glyoxal photolysis through channel 1a, HC(O)C(O) + H, would lead to the rapid formation of HCO via reaction 2, where $k_2(296\ \text{K}) = 3.2 \times 10^7$ s^{-1}.[18] Therefore, HCO formation via reaction 2 would appear to be instantaneous in our measurements. The decrease in HCO quantum yield at wavelengths <350 nm can be explained by either the opening up of the HC(O)C(O) + H channel or a decrease in the 2HCO channel and an increase in other photolysis channels, or both.

The photodynamics of glyoxal in the wavelength region of this work are complex, involving multiple photolysis products and multiple excited-state potential energy surfaces. Excited-state glyoxal may undergo intersystem crossing or internal conversion to another PES, and the rates for these processes may depend sensitively on the excitation energy, pressure, or both.[16,20,29−36] Our technique does not allow for a detailed investigation of the photodissociation dynamics but instead measures the overall ratio of the quenching to dissociation rate coefficients. Interpolated values of Φ^0_{HCO} at integral wavelengths in the wavelength range of 290−420 nm are listed in Table S2 in the Supporting Information. Interpolation of the data within the highly structured portion of the absorption spectrum was justified by the lack of any systematic dependence of Φ^0_{HCO} values on the excitation wavelength in this region. Using the interpolated Φ^0_{HCO} values and the $k_q/k_d(\lambda)$ parametrization given in eq 15, HCO quantum yields can be determined at specific wavelengths in the range of 290−420 nm and pressures with the Stern−Volmer relationship (eq 14).

Error Analysis. The uncertainty in $\Phi_{HCO}(\lambda,P)$ and the $\Phi^0_{HCO}(\lambda)$ and k_q/k_d values given in Table 2 were determined from the precision of the measurements and uncertainties in the parameters used in eq 9. Using the relative quantum yield method minimizes uncertainties associated with key measurement parameters such as the photolysis laser fluence, absorption path length, gas flow, and pressure, which are kept nearly constant during an experiment. The uncertainties in these parameters made only a small contribution to the overall uncertainty in $\Phi_{HCO}(\lambda,P)$. The precision of the CRDS time constant measurements was very high, ± 0.5%. The precision (2σ, 95% confidence intervals) from the least-squares fits used to determine $\Phi^0_{HCO}(\lambda)$ and k_q/k_d, eq 14, are given in Table 2 and include the uncertainty due to the correction for H_2CO photolysis. The linearity of HCO radical production was confirmed experimentally, ±5%, as shown in Figure S1 in the Supporting Information, over the same range of concentrations and photolysis laser fluences as that used in the quantum yield measurements. The precursor concentrations were measured online using calibrated flow rates and FT-IR spectroscopy. These measurements agreed to within 5%. We estimate the potential systematic uncertainties in $\Phi_{HCO}(\lambda,P)$ to be 12% at the 2σ (95% confidence) level.

Comparison with Previous Studies. HCO quantum yield measurements were previously made in the wavelength range of 290−420 nm by Chen and Zhu.[21] The Φ^0_{HCO} values from our work are in agreement, within experimental error, with those determined by Chen and Zhu, although the values from our work are generally systematically lower. The k_q/k_d ratios are, however, significantly different from those measured by Chen and Zhu.[21] First, we measure a nonzero value for k_q/k_d at wavelengths <380 nm, in contrast with the Chen and Zhu work. We also measure a substantially greater (factor of two) k_q/k_d ratio at wavelengths >400 nm. Figure 8 illustrates these differences, showing Chen and Zhu's atmospheric HCO quantum yield and that from this

TABLE 1: Results from a Stern−Volmer Analysis of the HCO Quantum Yield Data Obtained in the UV/vis Photolysis of Glyoxal[a]

λ(nm)[b]	Φ^0_{HCO}[c]	k_q/k_d (10^{-20} cm^3 molecule^{-1})	λ (nm)	Φ^0_{HCO}	k_q/k_d (10^{-20} cm^3 molecule^{-1})
290	0.38 ± 0.03	1.6 ± 2.2	355	1.63 ± 0.15	2.9 ± 0.6
297	0.44 ± 0.08	3.4 ± 2.9	356	1.53 ± 0.14	3.2 ± 0.6
300	0.44 ± 0.05	3.6 ± 2.9	357	1.58 ± 0.20	2.6 ± 0.7
302.5	0.50 ± 0.08	3.3 ± 3.4	358	1.58 ± 0.34	3.0 ± 1.2
308	0.65 ± 0.23	3.2 ± 6.9	359	1.57 ± 0.19	3.1 ± 0.8
311	0.62 ± 0.09	3.2 ± 3.2	360	1.61 ± 0.14	3.4 ± 0.5
313	0.74 ± 0.15	2.2 ± 3.2	361	1.65 ± 0.13	2.9 ± 0.5
316	0.95 ± 0.21	1.6 ± 2.4	362	1.55 ± 0.15	3.2 ± 0.6
319	0.85 ± 0.16	1.2 ± 2.3	363	1.62 ± 0.14	3.5 ± 0.6
320	0.99 ± 0.15	1.4 ± 1.6	364	1.65 ± 0.13	3.6 ± 0.5
321	1.17 ± 0.20	0.6 ± 1.4	365	1.68 ± 0.17	3.8 ± 0.6
322	1.12 ± 0.45	2.0 ± 3.1	366	1.70 ± 0.14	4.1 ± 0.5
323	1.08 ± 0.40	1.3 ± 2.0	367	1.61 ± 0.15	4.3 ± 0.6
324	1.17 ± 0.41	1.7 ± 1.8	368	1.72 ± 0.14	4.5 ± 0.5
325	1.15 ± 0.34	2.0 ± 2.1	369	1.66 ± 0.17	4.5 ± 0.6
327	1.22 ± 0.17	2.4 ± 1.5	370	1.85 ± 0.27	4.5 ± 2.5
328	1.35 ± 0.20	2.5 ± 1.2	371	1.79 ± 0.19	4.6 ± 0.6
329	1.39 ± 0.19	2.1 ± 1.1	372	1.70 ± 0.55	4.9 ± 2.0
330	1.68 ± 0.34	2.6 ± 1.6	373	1.73 ± 0.37	5.3 ± 1.3
331	1.46 ± 0.50	2.8 ± 1.7	374	1.74 ± 0.32	5.7 ± 1.2
332	1.69 ± 0.41	3.0 ± 1.4	375	1.77 ± 0.51	5.5 ± 1.8
333	1.73 ± 0.46	2.8 ± 1.4	376	1.72 ± 0.24	6.0 ± 0.9
334	1.64 ± 0.28	2.6 ± 1.2	377	1.77 ± 0.21	6.1 ± 0.8
335	1.58 ± 0.18	2.2 ± 0.9	378	1.75 ± 0.33	6.4 ± 1.2
336	1.59 ± 0.22	2.3 ± 1.0	379	1.83 ± 0.27	6.7 ± 0.9
337	1.72 ± 0.23	2.4 ± 0.8	380	1.80 ± 0.19	7.5 ± 0.6
338	1.70 ± 0.28	2.1 ± 0.8	381	1.77 ± 0.36	7.9 ± 1.2
339	1.61 ± 0.34	1.9 ± 1.0	382	1.77 ± 0.23	8.0 ± 0.8
340	1.87 ± 0.30	3.7 ± 1.8	383	1.80 ± 0.17	8.7 ± 0.6
341	1.43 ± 0.30	2.5 ± 1.7	384	1.80 ± 0.16	9.3 ± 0.6
342	1.43 ± 0.40	2.0 ± 2.3	385	1.80 ± 0.20	9.5 ± 0.7
343	1.38 ± 0.39	1.7 ± 2.2	386	1.72 ± 0.46	10.0 ± 1.7
344	1.64 ± 0.28	2.4 ± 1.2	387.035	1.66 ± 0.73	11.1 ± 2.8
345	1.94 ± 0.57	2.5 ± 2.0	388.038	1.65 ± 0.83	14.6 ± 3.4
346	1.77 ± 0.14	2.4 ± 0.5	389.042	1.65 ± 0.83	14.1 ± 3.3
347	1.69 ± 0.17	2.4 ± 0.6	390.046	1.69 ± 0.84	15.5 ± 3.6
348	1.59 ± 0.13	2.7 ± 0.6	391.049	1.56 ± 0.82	19.6 ± 3.9
349	1.56 ± 0.17	2.7 ± 0.7	392.053	1.20 ± 0.63	25.0 ± 5.1
350	1.74 ± 0.24	2.7 ± 1.2	398.96	0.80 ± 0.23	27.7 ± 4.8
351	1.80 ± 0.15	3.4 ± 0.5	400	0.87 ± 0.47	23.0 ± 8.0
352	1.78 ± 0.30	3.3 ± 1.1	408	0.43 ± 0.20	37.2 ± 15.0
353	1.72 ± 0.17	2.9 ± 0.6	416	0.14 ± 0.02	64.9 ± 10.1
354	1.56 ± 0.13	3.1 ± 0.6			

[a] Zero-pressure HCO quantum yields, Φ_0^{HCO}, and k_q/k_d values were obtained from weighted linear least-squares fits of experimental values obtained over the pressure range 50−500 Torr (N_2) at 296 K. The data tabulated here are also shown in Figures 6 and 7. [b] Photolysis wavelengths (in air) are accurate to 0.01 nm. [c] Quoted uncertainties represent the 2σ (95% confidence interval) precision from the Stern−Volmer analysis fits.

work plotted as a function of wavelength. In the wavelength range of 320−370 nm, the HCO quantum yield determined in this work is as much as a factor of two lower than that determined by Chen and Zhu. A possible explanation for this discrepancy is discussed in the following section (Secondary Production of HCO).

Tadic et al.[8] used broadband photolysis to examine the wavelength and pressure dependence of glyoxal quantum yields via measurements of stable end products. They reported a total quantum yield from the observed loss of glyoxal, a branching ratio for the sum of channels 1c and 1e, and the branching ratio for channel 1d. Combining their results with existing literature data, they estimated the wavelength dependence for each of the photolysis channels (1c, 1d, and 1e) at atmospheric pressure. The branching ratio results from the Tadic et al. study are illustrated in Figure 8. The wavelength dependence of the HCO quantum yield estimated by Tadic et al. is significantly different from that determined in this work. Specifically, our quantum yields are substantially lower at $\lambda < 360$ nm and greater at $\lambda > 360$ nm.

Secondary Production of HCO. During the course of our experiments, we discovered that excitation of glyoxal at wavelengths >400 nm, that is, below the expected energetic threshold for dissociation via channel 1c, lead to the production of HCO radicals through rapid secondary gas-phase chemistry. The observation of secondary HCO formation was unexpected. More specifically, this phenomenon was observed following excitation at several wavelengths >400 nm under conditions where the excitation of glyoxal into the first excited state was high. Secondary HCO formation was not observed for photolysis wavelengths <400 nm under the experimental conditions used in the present study. For photolysis wavelengths ≥400 nm, the HCO temporal profiles showed prompt HCO formation due to HCO production as a primary photolysis product followed by

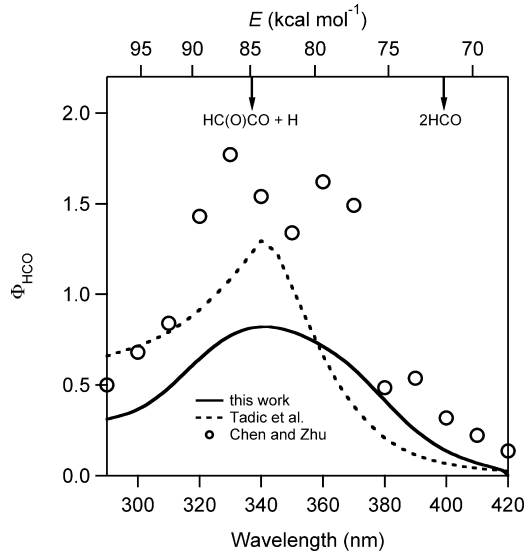

Figure 8. Comparison of HCO quantum yield values for glyoxal photolysis at atmospheric pressure from this work (solid line) and Chen and Zhu[21] (○). Also shown are the results from the analysis given by Tadic et al.[8] (dashed line) that is currently recommended for use in atmospheric models.[15] The vertical arrows represent the thermodynamic thresholds for photolysis channels 1a (HCOCO + H) and 1c (HCO + HCO).[15,16]

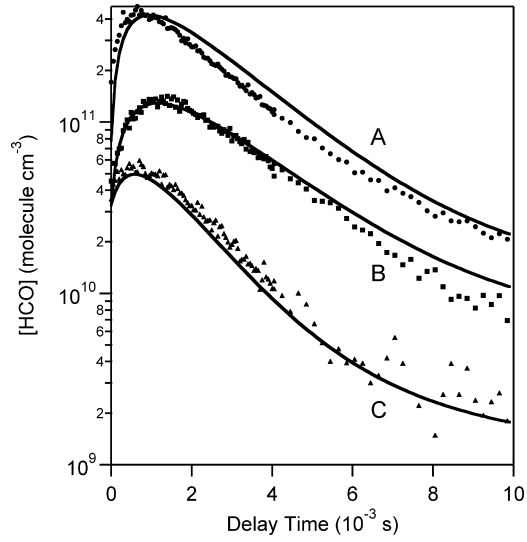

Figure 9. Representative HCO temporal profiles that illustrate the secondary production of HCO following photolysis of glyoxal at wavelengths >400 nm. The solid traces are results from a simple kinetic simulation in which the rate coefficient for glyoxal* + glyoxal* → 2HCO is equal to 2×10^{-10} cm^3 molecule^{-1} s^{-1}. The experimental conditions for the HCO temporal profiles shown are: (A) [glyoxal]$_0$ = 1.25×10^{15} molecules cm^{-3}, 100 Torr N_2, photolysis laser fluence = 4.0 mJ cm^{-2} pulse^{-1}, $\lambda_{photolysis}$ = 414.165 nm ($\sigma_{glyoxal} = 1.49 \times 10^{-19}$ cm^2 molecule^{-1}); (B) [glyoxal]$_0$ = 1.24×10^{15} molecules cm^{-3}, 100 Torr N_2, photolysis laser fluence = 1.7 mJ cm^{-2} pulse^{-1}, $\lambda_{photolysis}$ = 414.165 nm ($\sigma_{glyoxal} = 1.49 \times 10^{-19}$ cm^2 molecule^{-1}); (C) [glyoxal]$_0$ = 6.6×10^{14} molecules cm^{-3}, 300 Torr N_2, photolysis laser fluence = 4.0 mJ cm^{-2} pulse^{-1}, $\lambda_{photolysis}$ = 413.925 nm ($\sigma_{glyoxal} = 8.28 \times 10^{-20}$ cm^2 molecule^{-1}).

a rapid rise, $(0.2-1.1) \times 10^4$ s^{-1}, and a subsequent slower decay. It was confirmed that the increase in absorption signal was indeed due to HCO by tuning the probe laser off the peak of the HCO absorption feature. Figure 9 shows several representative HCO temporal profiles recorded for ~414 nm photolysis under different experimental conditions.

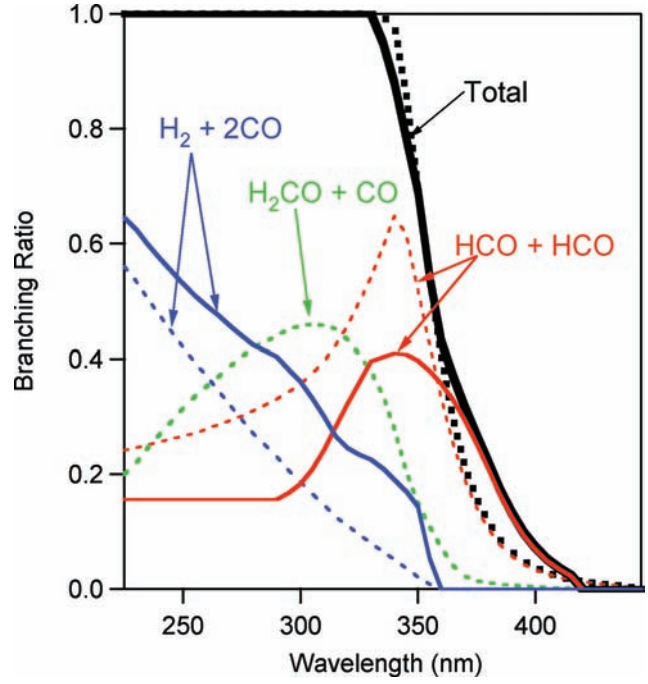

Figure 10. Revision of the glyoxal photolysis product branching ratio at 1 atm total pressure and 298 K on the basis of the HCO quantum yields obtained in this study. The dashed lines show the product branching ratios taken from Tadic et al.,[8] which are currently recommended for use in atmospheric models. The values for the H_2 + 2CO and 2HCO channels (solid lines) were obtained from this work, as described in the text. The revised product branching ratios for each channel are given in Table 2.

The thermodynamic threshold for glyoxal dissociation to form two HCO radicals is well established and corresponds to excitation at 398.8 nm.[15] However, HCO is observed as a primary photolysis product at wavelengths >400 nm (below the threshold energy). The observed initial HCO signal presumably originates from ground-state molecules with internal excitation. The observed HCO production in the temporal profiles is suggestive of an energy pooling reaction between glyoxal molecules in the T_1 state. Two T_1 glyoxal molecules contain sufficient energy, 109.8 kcal mol^{-1}, which is well above the energetic threshold to form 2HCO radicals, 72.5 kcal mol^{-1}

$$\mathrm{HCOCOH(T_1) + HCOCOH(T_1) \rightarrow 2HCO + HCOCOH(S_0) + 37.3\ kcal\ mol^{-1}} \quad (16)$$

We tested this hypothesis by performing experiments over a range of conditions including variations in total pressure, photolysis laser fluence, excitation wavelengths, and glyoxal concentrations. The rate of secondary HCO production primarily correlated with the concentration of initial glyoxal electronically excited, [glyoxal*]$_0$, where [glyoxal*]$_0$ = [glyoxal] $\sigma_g(\lambda)$ $F(\lambda)$. Secondary HCO production was not observed when [glyoxal*] $< 2 \times 10^{11}$ molecules cm^{-3}. Only two photolysis wavelengths in the range from 405 to 420 nm had absorption cross sections low enough to achieve this condition: 408 and 416 nm. A simple kinetic mechanism including reaction 16 with $k_{16} = 2 \times 10^{-10}$ cm^3 molecule^{-1} s^{-1} and a first-order HCO loss (e.g., reaction 12) reproduced the observed HCO temporal profiles reasonably well, as shown in Figure 9. This analysis suggests that the energy pooling reaction is extremely efficient. However, some systematic deviations from this simple model are observed for the

TABLE 2: Wavelength-Dependent Product Branching Yields for the UV/vis Photolysis of Glyoxal at Atmospheric Pressure (760 Torr) and 298 K for Use in Atmospheric Model Calculations[a]

λ (nm)	$\Phi_{1c}^{Atm}(\lambda)$ 2HCO	$\Phi_{1d}^{Atm}(\lambda)$ $H_2CO + CO$	$\Phi_{1e}^{Atm}(\lambda)$ $H_2 + 2CO$	λ (nm)	$\Phi_{1c}^{Atm}(\lambda)$ 2HCO	$\Phi_{1d}^{Atm}(\lambda)$ $H_2CO + CO$	$\Phi_{1e}^{Atm}(\lambda)$ $H_2 + 2CO$
225	0.156	0.199	0.645	325	0.358	0.408	0.234
230	0.156	0.219	0.625	330	0.396	0.379	0.225
235	0.156	0.245	0.599	335	0.403	0.337	0.210
240	0.156	0.269	0.575	340	0.410	0.279	0.190
245	0.156	0.291	0.553	345	0.408	0.204	0.170
250	0.156	0.314	0.530	350	0.397	0.150	0.144
255	0.156	0.334	0.510	355	0.379	0.108	0.053
260	0.156	0.352	0.492	360	0.357	0.072	0
265	0.156	0.369	0.475	365	0.329	0.040	0
270	0.156	0.387	0.457	370	0.294	0.022	0
275	0.156	0.404	0.440	375	0.253	0.014	0
280	0.156	0.420	0.424	380	0.208	0.011	0
285	0.156	0.430	0.414	385	0.164	0.008	0
290	0.156	0.440	0.404	390	0.125	0.007	0
295	0.167	0.451	0.382	395	0.093	0.005	0
300	0.183	0.457	0.360	400	0.068	0.004	0
305	0.208	0.460	0.332	405	0.049	0.003	0
310	0.242	0.458	0.300	410	0.035	0.002	0
315	0.282	0.452	0.266	415	0.023	0.001	0
320	0.322	0.433	0.245	420	0	0	0

[a] Values are shown and compared with the previous recommendation[15] in Figure 10.

highest levels of $[glyoxal^*]_0$. The actual reaction mechanism is therefore most likely more complex than that used here, but the present analysis confirms that excited-state chemistry can account for the observed HCO formation. We should point out that in the atmosphere, energy pooling between excited glyoxal will not be significant because the lifetime of glyoxal in T_1 will be much shorter than the time between collisions of excited glyoxal molecules.

Interestingly, this is not the first report of gas-phase glyoxal excited-state chemistry. In 1964, Parmenter[35] found that when glyoxal−acetaldehyde mixtures were irradiated at 435.8 nm, methane was formed at 153 °C but not at 37 °C. Because no methane was observed at 37 °C, it is unlikely that a glyoxal* + acetaldehyde reaction would be the source of the methane. The methane yields were also shown to have no time dependence, ruling out the possibility that the source of the CH_4 is a stable glyoxal photolysis product. The formation of methane was attributed to the following radical chemistry

$$R + CH_3C(O)H \rightarrow RH + CH_3CO \quad (17)$$

$$CH_3CO \rightarrow CH_3 + CO \quad (18)$$

$$CH_3 + CH_3C(O)H \rightarrow CH_4 + CH_3CO \quad (19)$$

$$2\,CH_3 \rightarrow C_2H_6 \quad (20)$$

where R is an unknown radical. It was shown that the formation of R most likely occurred via reaction of two excited glyoxal molecules. The identity of the radical R was not established, but our results would suggest that R = HCO.

The HCO quantum yield values reported in this work at 408 and 416 nm were obtained under conditions with no observable secondary HCO production. However, glyoxal excited-state chemistry and the subsequent rapid formation of HCO may explain the discrepancies between our quantum yield results and those of Chen and Zhu[21] at wavelengths >400 nm. On the basis of the analysis above, we estimate that for the conditions used in the Chen and Zhu experiments, [glyoxal*] was $\sim 10^{13}$ molecules cm^{-3}. This is approximately 100 times higher than that estimated for the HCO temporal profiles shown in Figure 9. Such high levels of excitation would result in the very rapid (<10 μs) secondary formation of HCO radicals via reaction 16 and lead to a systematic overestimate of the HCO quantum yield. For example, under the conditions of our experiments, extrapolation of the HCO signals shown in Figure 9 back to $t = 0$ could result in an overestimate in $\Phi_{HCO}(\lambda,P)$ by a factor of four or greater. A comparison of our Φ^0_{HCO} at 416 nm (0.05) versus the Chen and Zhu value at 420 nm (0.5) is reconciled with this interpretation.

Atmospheric Implications. The UV/vis photolysis of oxygenated volatile organic compounds (OVOCs) such as glyoxal plays an important role in determining the oxidative capacity of the atmosphere from the Earth's surface throughout the entire troposphere. Two key factors needed to describe an OVOC's atmospheric photoysis are: (1) the overall photolysis rate, which establishes its atmospheric lifetime, and (2) the rate of radical production or, in other words, the photolysis product yields. In many cases, both processes are dependent on pressure and, therefore, vary as a function of altitude. The measurements in this work provide a comprehensive data set of HCO quantum yields over the wavelength range important for atmospheric photolysis calculations. The present study provides accurate HCO quantum yield data for the photolysis of glyoxal and enables the refinement of recommendations for atmospheric models. This discussion will focus on the radical production channels and a reinterpretation of the wavelength-dependent photolysis product branching ratios, as given by Tadic et al.,[8] which are the values currently recommended for use in atmospheric models.[15]

Using the recommended values for the product yields put forth by Tadic et al.,[8] we have incorporated our results and provided a new recommendation, as shown in Figure 10 and Table 2. It should be noted that photolysis channel 1a may have a significant branching ratio at energies above its thermodynamic threshold (λ < 337 nm). However, channel 1a results in the rapid formation of HCO via unimolecular decomposition of the HCOCO radical (reaction 2), which is instantaneous on the time

scale of our measurements and under atmospheric boundary layer conditions. Therefore, for wavelengths <337 nm, our HCO quantum yield is most likely a combination of channels 1a and 1c, although we treat the branching ratio for atmospheric modeling to be entirely due to channel 1c.

The Tadic et al.[8] work estimated branching ratios for the photolysis of glyoxal by monitoring the loss of glyoxal and formation of stable end products such as H_2CO and CO following broadband photolysis of glyoxal in 760 Torr of air. Channel 1d resulted in unique end products, but channels 1c and 1e were indistinguishable in the Tadic et al. work. Because these channels could not be distinguished, the earlier works of Chen and Zhu[21] and Calvert and Lane[23] were combined with the broadband results to provide a recommendation for channels 1c, 1d, and 1e (Figure 10).

We made our revision to the branching ratios by replacing the Tadic et al.[8] values for channel 1c with our parametrized HCO yields at 760 Torr and then adjusting channel 1e accordingly to maintain the same recommended total value. These revised values provide the best estimate of the product branching ratios for the UV/vis photolysis of glyoxal at atmospheric pressure and are intended for use in atmospheric model calculations. Figure 10 shows the revised values for the branching ratios in the UV/vis photolysis of glyoxal at atmospheric pressure. At wavelengths >360 nm, the results from our work show that channel 1c contributes greater than the recommended total yield, and as a result, we have revised the total yield to higher values. Also note that channel 1d was determined by Tadic et al.[8] to have a minor, but nonzero, branching ratio in the wavelength range from 340 to 380 nm. This is qualitatively consistent with our result that Φ^0_{HCO} does not reach its maximum allowable value of 2 in this wavelength range. Finally, the increase in channel 1e at shorter wavelengths is roughly correlated with the observed decrease in channel 1c. Therefore, the opening of channel 1e is a possible explanation for the observed decrease in Φ^0_{HCO} at wavelengths <340 nm. However, as discussed above, the opening of channel 1a, which was not explicitly included in our analysis, could also account for this behavior.

Finally, we need to point out that the technique used in this study to determine the HCO quantum yield does not allow the use of O_2 as a bath gas because of the rapid reaction with the HCO radical, (eq 12). Therefore, the role of O_2 as a collisional quencher was not investigated. The results from the Tadic et al.[8] experiments, which were performed in air, are in reasonable agreement with our work, suggesting that O_2 does not have substantially different quenching properties than N_2. However, studies involving O_2 as well as temperature-dependent quantum yield studies are desired to provide a more complete understanding of the photochemistry of glyoxal under atmospheric conditions.

Acknowledgment. This work was partially funded by NOAA's Health of the Atmosphere and Air Quality programs and by NASA's Atmospheric Composition program.

Supporting Information Available: HCO quantum yield data used in the Stern−Volmer analysis at each photolysis wavelength, HCO zero-pressure quantum yields at 1 nm intervals over the wavelength range of 290−420 nm for use in atmospheric models obtained using the parametrizations given in the text, and representative data showing the experimentally observed linearity of the HCO signal with photolysis laser fluence and initial glyoxal concentration. This material is available free of charge via the Internet at http://pubs.acs.org.

References and Notes

(1) Carter, W. P. L.; Atkinson, R. *Int. J. Chem. Kinet.* **1996**, *28*, 497.
(2) Ham, J. E.; Proper, S. P.; Wells, J. R. *Atmos. Environ.* **2006**, *40*, 726.
(3) Magneron, I.; Thevenet, R.; Mellouki, A.; Le Bras, G.; Moortgat, G. K.; Wirtz, K. *J. Phys. Chem. A* **2002**, *106*, 2526.
(4) Nunes, F. M. N.; Veloso, M. C. C.; Pereira, P.; de Andrade, J. B. *Atmos. Environ.* **2005**, *39*, 7715.
(5) Volkamer, R.; Platt, U.; Wirtz, K. *J. Phys. Chem. A* **2001**, *105*, 7865.
(6) Feierabend, K. J.; Zhu, L.; Talukdar, R. K.; Burkholder, J. B. *J. Phys. Chem. A* **2008**, *112*, 73.
(7) Plum, C. N.; Sanhueza, E.; Atkinson, R.; Carter, W. P. L.; Pitts, J. N. *Environ. Sci. Technol.* **1983**, *17*, 479.
(8) Tadic, J.; Moortgat, G. K.; Wirtz, K. *J. Photochem. Photobiol., A* **2006**, *177*, 116.
(9) Volkamer, R.; Molina, L. T.; Molina, M. J.; Shirley, T.; Brune, W. H. *Geophys. Res. Lett.* **2005**, *32*, L08806.
(10) Munger, J. W.; Jacob, D. J.; Daube, B. C.; Horowitz, L. W.; Keene, W. C.; Heikes, B. G. *J. Geophys. Res.* **1995**, *100*, 9325.
(11) Spaulding, R. S.; Schade, G. W.; Goldstein, A. H.; Charles, M. J. *J. Geophys. Res.* **2003**, *108D*, 4247.
(12) Huisman, A. J.; Hottle, J. R.; Coens, K. L.; DiGangi, J. P.; Galloway, M. M.; Kammrath, A.; Keutsch, F. N. *Anal. Chem.* **2008**, *80*, 5884.
(13) Wittrock, F.; Richter, A.; Oetjen, H.; Burrows, J. P.; Kanakidou, M.; Myriokefalitakis, S.; Volkamer, R.; Beirle, S.; Platt, U.; Wagner, T. *Geophys. Res. Lett.* **2006**, *33*, L16804.
(14) Myriokefalitakis, S.; Vrekoussis, M.; Tsigaridis, K.; Wittrock, F.; Richter, A.; Bruhl, C.; Volkamer, R.; Burrows, J. P.; Kanakidou, M. *Atmos. Chem. Phys.* **2008**, *8*, 4965.
(15) Sander, S. P.; Finlayson-Pitts, B. J.; Friedl, R. R.; Golden, D. M.; Huie, R. E.; Keller-Rudek, H.; Kolb, C. E.; Kurylo, M. J.; Molina, M. J.; Moortgat, G. K.; Orkin, V. L.; Ravishankara, A. R.; Wine, P. H. *Chemical Kinetics and Photochemical Data for Use in Atmospheric Studies, Evaluation Number 15*; JPL Publication 02-25; NASA Jet Propulsion Laboratory, California Institute of Technology: Pasadena, CA, 2006.
(16) Li, Q. S.; Zhang, F.; Fang, W. H.; Yu, J. G. *J. Chem. Phys.* **2006**, *124*, 054324.
(17) Koch, D. M.; Khieu, N. H.; Peslherbe, G. H. *J. Phys. Chem. A* **2001**, *105*, 3598.
(18) Orlando, J. J.; Tyndall, G. S. *Int. J. Chem. Kinet.* **2001**, *33*, 149.
(19) Hepburn, J. W.; Buss, R. J.; Butler, L. J.; Lee, Y. T. *J. Phys. Chem.* **1983**, *87*, 3638.
(20) Chen, M.-W.; Lee, S. J.; Chen, I.-C. *J. Chem. Phys.* **2003**, *119*, 8347.
(21) Chen, Y. Q.; Zhu, L. *J. Phys. Chem. A* **2003**, *107*, 4643.
(22) Zhu, L.; Kellis, D.; Ding, C. F. *Chem. Phys. Lett.* **1996**, *257*, 487.
(23) Calvert, J. G.; Layne, G. S. *J. Am. Chem. Soc.* **1953**, *75*, 856.
(24) Flad, J. E.; Brown, S. S.; Burkholder, J. B.; Stark, H.; Ravishankara, A. R. *Phys. Chem. Chem. Phys.* **2006**, *8*, 3636.
(25) Volkamer, R.; Spietz, P.; Burrows, J.; Platt, U. *J. Photochem. Photobiol., A* **2005**, *172*, 35.
(26) Maric, D.; Burrows, J. P.; Meller, R.; Moortgat, G. K. *J. Photochem. Photobiol., A* **1993**, *70*, 205.
(27) Ninomiya, Y.; Goto, M.; Hashimoto, S.; Kagawa, Y.; Yoshizawa, K.; Kawasaki, M.; Wallington, T. J.; Hurley, M. D. *J. Phys. Chem. A* **2000**, *104*, 7556.
(28) Nakanaga, T.; Kondo, S.; Saeki, S. *J. Chem. Phys.* **1982**, *76*, 3860.
(29) Anderson, L. G.; Parmenter, C. S.; Poland, H. M. *Chem. Phys.* **1973**, *1*, 401.
(30) Beyer, R. A.; Lineberger, W. C. *J. Chem. Phys.* **1975**, *62*, 4024.
(31) Beyer, R. A.; Zittel, P. F.; Lineberger, W. C. *J. Chem. Phys.* **1975**, *62*, 4016.
(32) Burak, I.; Hepburn, J. W.; Sivakumar, N.; Hall, G. E.; Chawla, G.; Houston, P. L. *J. Chem. Phys.* **1987**, *86*, 1258.
(33) Kao, C. C.; Ho, M. L.; Chen, M. W.; Lee, S. J.; Chen, I. C. *J. Chem. Phys.* **2004**, *120*, 5087.
(34) Loge, G. W.; Parmenter, C. S. *J. Phys. Chem.* **1981**, *85*, 1653.
(35) Parmenter, C. S. *J. Chem. Phys.* **1964**, *41*, 658.
(36) Yardley, J. T. *J. Chem. Phys.* **1972**, *56*, 6192.

JP9033003